Carbohydrate Polymers 216 (2019) 360–368

Contents lists available at ScienceDirect

Carbohydrate Polymers

journal homepage: www.elsevier.com/locate/carbpol

Nanocellulose as a colorimetric biosensor for effective and facile detection of human neutrophil elastase

Zhe Ling[a,b], Feng Xu[a,*], J. Vincent Edwards[b,*], Nicolette T. Prevost[b], Sunghyun Nam[b], Brian D. Condon[b], Alfred D. French[b]

[a] Beijing Key Laboratory of Lignocellulosic Chemistry, Beijing Forestry University, Beijing 100083, PR China
[b] Southern Regional Research Center, Agricultural Research Service, USDA, 1100 Robert E. Lee Blvd., New Orleans, LA 70124, USA

ARTICLE INFO

Keywords:
DES treatment
Cotton cellulose nanocrystals
Wood cellulose nanofibrils
Biosensors
Human neutrophil elastase (HNE) peptide

ABSTRACT

Nanocellulose has functionalities suitable for efficient sensor transducer surface design including crystallinity, biocompatible and high specific surface area. Here we explore two forms of nanocellulose as transducer surfaces to enable colorimetric detection of human neutrophil elastase (HNE), and a wide range of inflammatory diseases. A deep eutectic solvent (DES) was utilized to mediate formation of cotton cellulose nanocrystals (DCNCs) employed to prepare a peptide-cellulose conjugate as a protease sensor of HNE. The tetrapeptide-cellulose analog on DCNC is contrasted with an analogous derivative of TEMPO-oxidized wood cellulose nanofibrils (WCNFs). DCNCs showed greater degree of substitution of HNE tetrapeptide and sensitivity to the elastase than WCNFs, despite the smaller surface area and pore sizes. XRD models revealed the higher crystallinity and larger crystallite sizes of DCNCs, indicating the well-arranged cellulose chains for immobilization of the tetrapeptide on (110) lattice reflections of cellulose crystals. The sensitivity of DCNCs-based colorimetric sensor was less than 0.005 U/mL, which would provide a convenient, sensitive sensor applicable for improved colorimetric point of care protease biomarker detection.

1. Introduction

Nanocellulose-based materials have widespread interest for their renewable, sustainable, nontoxic, biodegradable, thermal and chemical stability (Habibi, Lucia, & Rojas, 2010; Wang, Lu, & Zhang, 2016). Moreover, the applications of nanocellulose in the biomedical area are growing rapidly (Jorfi & Foster, 2015). In this regard, the actual application of cellulose and nanocellulose to the development of biosensor transducer surfaces has received increased attention in recent years (Edwards, Prevost, Sethumadhavan, Ullah, & Condon, 2013). This is especially the case with protease sensors where the goal is point of care diagnostics interfaced with wound care treatment of chronic wounds, and a timely topic for clinical translation research as relates to protease modulating dressings to chronic wound treatment (Edwards, Fontenot, Prevost et al., 2016; Romanelli, Miteva, Romanelli, Barbanera, & Dini, 2013; Serena et al., 2016). Although, some approaches to point of care protease diagnostics and treatment have been adopted internationally as a clinical point of care tool, the use of protease sensors as guides to chronic wound treatment have not been completely realized worldwide. This in part is due to an incomplete understanding of the complexity of chronic wound types where variable protease levels have demonstrated less than a predictable certainty correlating to a trajectory to wound healing in different wound types and thus a choice of appropriate dressings to treat pathological protease levels (Dabiri, Damstetter, & Phillips, 2016). Nonetheless, as research in this area strengthens the paradigm of monitoring protease activity, basic to protease sensor design and development is the balance of protease sensor detection sensitivity and selectivity with optimization of dressing treatment. Thus, fundamental questions regarding approaches to protease detection and treatment are currently based on the surface chemistry of dressing/sensor interface design and transducer surfaces consisting of nanocellulosic materials, which provides a platform for adopting point of care protease sensors for chronic wound treatment, and other inflammatory diseases where proteases biomarker are central to disease diagnostics or theranostics. (Edwards, Fontenot, Prevost et al., 2016; Salas, Nypelö, Rodriguez-Abreu, Carrillo, & Rojas, 2014).

Human neutrophil elastase (HNE) is a serine protease central to the pathology in a wide range of diseases including chronic wounds, cystic fibrosis, and acute respiratory distress syndrome (Owen, 2008). Although neutrophil proteases are necessary for completion of wound

* Corresponding authors.
E-mail addresses: jjling814@bjfu.edu.cn (Z. Ling), xfx315@bjfu.edu.cn (F. Xu), vince.edwards@ars.usda.gov (J.V. Edwards), nicolette.prevost@ars.usda.gov (N.T. Prevost), sunghyun.nam@usda.gov (S. Nam), al.french@usda.gov (A.D. French).

https://doi.org/10.1016/j.carbpol.2019.04.027
Received 4 December 2018; Received in revised form 18 March 2019; Accepted 5 April 2019
Available online 08 April 2019
0144-8617/

healing, HNE is secreted in high titre from neutrophils in the inflammatory stage of chronic wounds, and the high concentration of HNE in chronic wounds is responsible for the breakdown of growth factors and connective tissue proteins contributing to non-healing wounds. The mechanism of action is similar to the role HNE plays in the pathophysiology of other inflammatory diseases (Yager et al., 1997). Thus, point of care protease detection of HNE has received increased attention for its clinical relevance to chronic wounds and other inflammatory diseases where expedited determination of the role of proteases in pathophysiology is critical to patient care. Previously we have assessed the relative roles of HNE substrate sensitivity by examining use of fluorogenic and chromogenic signal transduction on a wide range of cellulosic and nanocellulosic matrices (Edwards et al., 2013; Fontenot et al., 2017). In this manner, improvement in protease sensor sensitivity has been shown by enhancing substrate-enzyme recognition properties, and increasing the specific surface area of the transducer surface and the employment of colorimetric amplification and spectroscopic sensitivity with fluorescence has been assessed (Fontenot et al., 2016). More recently assessing the peptide-cellulose conjugate in terms of the relative conformational contributions of the crystalline cellulose and the peptides conformation to the spatio-temporal influences of enzyme substrate kinetics has provided insights on design approaches to protease sensors at a molecular level (Edwards, Fontenot, Liebner, French, & Condon, 2018).

To further improve the surface properties of nanocellulose, we examined the use of oxalic acid/choline treatments of cotton cellulose as an adjunct treatment to forming cotton-based nanocellulose (Ling, Edwards et al., 2018; Ling, Zhang, Yang, Takabe, & Xu, 2018). The nanocellulose derived from new kind of DES treatment may provide new strategy on controlling the properties of the nanocellulose, such as the crystal sizes, content of carboxyl groups as well as the surface area, which are critical for improving the quality of the fabricated HNE sensor. Here we describe the preparation, characterization and activity of chromogenic analogs as HNE substrate, peptide-cellulose conjugates to form a nanocellulosic transducer surface with enhanced sensor sensitivity to HNE.

2. Experimental

2.1. Materials

The chemicals N,*N*-dimethylformamide (DMF), Ethylcyanogly oxylate-2-oxime (Oxyma Pure), Diisopropylcarbodiimide (DIC), 4-dimethylaminopyridine (DMAP) ChCl, trifluoroacetic acid (TFA) and triisopropylsilane were purchased from Sigma Aldrich (St. Louis, MO, USA). 9-fluorenylmethoxycarbonyl-glycine (Fmoc-glycine) was purchased from Peptides International and OA was purchased from JT Baker. The substrate AAPVpNA and HNE were purchased from Athens Research Technologies. All chemicals used in this study were either analytical or reagent grade. Raw cotton fibre was obtained from USDA-ARS storage and it was passed through a 60 mesh screen on a Wiley mill (Thomas-Wiley Mill Co.). WCNFs suspension (3%) and freeze dried powder made from softwood by TEMPO-oxidation were supplied by the University of Maine Process Development Center.

2.2. DES treatment and fabrication of cotton CNC

The ChCl and OA were mixed with molar ratios of 1:3. The DES was synthesized at 80 °C in a round bottom flask for 1 h until a clear viscous liquid was obtained. Then, 1 g of bleached cotton cellulose was added into 100 mL of the clear liquid with magnetic stirring for 2 h at 80°C. The mixture was then filtered and thoroughly washed by acetone and deionized water to neutral pH. The treated cellulose was mixed in deionized water followed by a high-power ultrasonic homogenizer (MSK-USP-3 N) with maximum of 300 W, 20 kHz. The resulting 0.5 wt. % cotton CNC suspension was lyophilized by a Freezemobile 25XL freeze dryer (VirTis, Gardiner) for 48 h. The freeze dried powder was denoted as DCNC.

2.3. Esterification of matrices

Standard fluorenylmethyloxycarbonyl (Fmoc) chemistry was used for esterification and immobilization of the peptide onto the matrices. (Sibrian-Vazquez, Jensen, Hammer, & Vicente, 2006) Briefly, Oxyma Pure (0.05 *g*, 0.3 mmol), DIC (0.048 mL, 0.3 mmol) and DMAP (0.035 *g*, 0.3 mmol) in DMF with Fmoc-Gly (0.075 *g*, 0.3 mmol) were added into a 50 mL centrifuge tube. The DCNCs and WCNFs (0.5 *g*, 3 mmol) were respectively placed and the dispersions were sonicated for 3 h at 25–30 °C. The esterified NC-Gly-Fmoc were washed thrice with DMF and allowed to remain in DMF for storage at 4–8 °C. Prior to immobilization of the tetrapeptide, the glycine groups were deprotected by soaking NC-Gly-Fmoc with 20% piperidine/DMF solution and agitating for 3, 5 and 7 min while washing with DMF after each time period. The obtained substrates were denoted as DCNC-gly and WCNF-gly and were then washed thrice with DMF followed by preparation for peptide coupling.

2.4. Immobilization of HNE peptide

Oxyma Pure (0.05 *g*, 0.3 mmol), DIC (0.048 mL, 0.3 mmol) and DMAP (0.035 *g*, 0.3 mmol) were added in minimal DMF, as well as the tetrapeptide AAPVpNA (0.1787 *g*, 0.3 mmol). The NC-Gly prepared previously (0.3 mmol) were placed in the 50 mL centrifuge tubes with the solution. The centrifuge tubes were placed in an ultrasonic bath while maintaining the temperature at 25–30 °C for 3 h and then placed in the refrigerator overnight. The NCs with peptide attached were respectively called DCNC-pep and WCNF-pep.

Upon the completion of drying, the peptide was cleaved from 10 mg of each biosensor by adding a mixture of TFA/water/triisopropylsilane (95/2.5/2.5) to the biosensor for three hours. The solutions were diluted with water (1:10) and submitted for electrospray ionization liquid chromatography mass spectrometry (ESI-LC/MS) to confirm the peptide component cleaved from the biosensor via its molecular weight.

2.5. Characterizations

Atomic force microscopy (AFM) analyses for DCNC and WCNF suspensions were conducted using an Agilent AFM series 5500 (Agilent Technologies) instrument. Zeta potential of DCNC was calculated by a Nano-ZS90 zeta-sizer and the data of WCNF was provided by the University of Maine. Chemical structure was determined by attenuated total reflectance FTIR (ATR-FTIR) spectroscopy (Bruker Optics, Billerica) and Raman spectroscopy (DXR2, Thermo Fisher Scientific). The elemental analysis of the solid matrices was performed by Midwest Microlabs and calculated as previously reported. (Edwards, Fontenot, Prevost et al., 2016). SSA and pore size were calculated from a 40-point nitrogen adsorption isotherm utilizing a TriStar II Plus 2.02 (Micromeritics, Norcross). Morphologies of the matrices were observed with a FEI Quanta 3D FEG FE-SEM. The accelerating potential was 5 kV, with a beam current of 20 mA.

XRD measurements were performed at room temperature with a PANalytical Empyrean diffractometer using Cu Kα-radiation (1.5418 Å). The patterns were analyzed using the pseudo-Voigt peak shape with the Maud Rietveld program (Materials Analysis Using Diffraction, version 2.7). Rietveld analysis of cellulosic materials requires a proposed model for the crystalline phases and some description of the amorphous phase. The crystalline phase was based on the crystal information file (.cif) for cellulose Iβ (French, 2014) that was a slightly modified version of the. cif provided by Nishiyama et al (Nishiyama, Langan, & Chanzy, 2002). The amorphous phase was based on the. cif for cellulose II with a small crystallite size (12 Å) as described before (French, 2014; Langan, Nishiyama, & Chanzy, 2001; Nam, French, Condon, & Concha, 2016). The crystallinity was calculated from the

area of the calculated pattern for crystalline cellulose divided by the sum of the areas for crystalline and amorphous regions. The d-spacings were calculated from refined unit cell dimensions and crystallite sizes perpendicular to different lattice planes were calculated using the Scherrer Eq. (1).

$$L_{hkl} = \frac{0.9\lambda}{B_{hkl}\cos\theta} \quad (1)$$

where λ is the X-Ray wavelength; B_{hkl} is the angular full-width at half maximum intensity (FWHM) in radians of the (*hkl*) line profile calculated by the fitted cellulose Iβ pattern in Origin (Microcal software version 7.0) ; θ is the scattering angle (Holzwarth & Gibson, 2011).

The chromogenic enzyme assay and colorimetric amplification reaction were conducted in duplicate. Each biosensor (1 mg) was placed into a 96-well plate and 1 mL of PBS (0.5 M NaCl and 0.1 M NaH_2PO_4, pH = 7.3) was added. A standard curve was constructed by employing peptide substrate solutions at concentrations of 0.005 μmol/mL and 0.15 μmol/mL with 0.05 mL 0.5U/mL HNE. Color amplification response was monitored with HNE concentration from 0.005 U/ mL to 0.2 U/ mL for 30 min reaction. Standard peptide substrates of 0.02, 0.08 and 0.2 μmol/mL were compared. The 96-well plate was shaken before each measurement in microplate reader and the measurements were acquired at a wavelength of 405 nm.

2.6. Molecular modelling studies

Computational studies were performed to calculate the minimization for the energy of tetrapeptide (Suc-AAPVpNA) anchored to the cellulose model compound cellotriose. The peptide substrate models were built using GaussView 5.0 (Gaussian Inc., Wallingford, CT, USA) and optimized using B3LYP6-31 + G* contained in the Gaussian 16 software.

3. Results and discussion

3.1. Preparation of biosensors and structure characterization

The immobilization reactions of the HNE substrate peptide with the cotton and wood nanocellulose are shown in Fig. 1c. The chemistry employed to form the peptide-cellulose conjugates on DCNC and WCNF has been previously described and employs the glycine-cellulose ester to attach by way of formation of an amide bond with the derivatized chromogentic tetrapeptide which reacts with a succinyl group at the amino-terminal of the glycine-cellulose ester. Thus the attachment of Suc-Ala-Ala-Pro-Val-pNa to the alpha-amino-cellulose ester yields the peptide-conjugate formed in both the cotton and wood nanocellulose. To confirm formation of the peptide-cellulose conjugate the ester bond between the glycine and cellulose was hydrolyzed and the resulting product confirmed as Gly-Succinyl-Ala-Ala-Pro-Val-pNa by way of mass spectroscopy (mass spec parent ion [M + H] = 634.28, Fig S1) correlating with the structure shown in Fig. 1. Mass spectroscopy peaks at 549.23 and 601.96 are ascribed to amino acid derivatives released during the TFA-mediated cellulose ester hydrolysis resulting in smaller truncated peptides (Eshraghi & Chowdhury, 1993).

AFM images of DCNCs and WCNFs in suspension are shown in Fig. 1a and b. Both forms of nanocellulose demonstrated homogeneous dispersion, and this phenomenon has been noted previously to correlate to negative charge distribution conferred by oxalic acid and derivatization by Tempo oxidation, respectively (B. Li et al., 2015; Sirviö, Visanko, & Liimatainen, 2016). Intact rod-like crystalline particles were found for cellulose resulting from the ChCl/OA treatments. The lengths of the DCNCs were approximately 100–200 nm (Fig. 1a). It is evident that there are also larger particles due to aggregation during freeze drying which is consistent with previous results (Ling, Edwards et al., 2018; Ling, Zhang et al., 2018). It is also notable that the presence of carboxyl groups at C6 in both nanocellulose analogs reduces the mechanical energy during mechanical grinding of the samples which has an effect on increasing specific surface area.

3.2. Chemical structural variations during the immobilization

ATR-FTIR and Raman spectra contrast the chemical structure of NCs and the linkage of the peptide analogs on the surface of the NCs (Fig. 2). ATR-FTIR spectra showed the typical cellulose peaks at 1430 cm^{-1}, 1376 cm^{-1}, 2900 cm^{-1}, confirming retention of crystalline regions of cellulose following immobilization of the peptide (Ling, Chen, Zhang, & Xu, 2017) The band at 1600 cm^{-1} and 1653 cm^{-1} are assigned to the carboxyl groups, which overlap with the C—C stretching band at 1604 cm^{-1} (Chung, Lee, & Choe, 2004; Liao, Lien, Shieh, Chen, & Lin, 2002). Those bands are more visible for WCNFs, indicating more carboxyl groups in TEMPO oxidized WCNFs than for DES treated DCNCs. The C—C stretching band right shifted in spectra of DCNC samples, possibly resulting from the absorbed water at 1640 cm^{-1} (Fig. 2a). Coincidently, the amide peaks assigned to the tetrapeptide conjugate are located at about 1650–1652 cm^{-1} (Edwards, Fontenot, Haldane et al., 2016; Orlandin, Formaggio, Toffoletti, & Peggion, 2014). The increasing intensity of this broad overlapped peak indicates the facile attachment of glycine or tetrapeptide on NC samples.

Raman spectra provided additional information on chemical variations of NC samples. For the untreated NCs, WCNF had more carboxyl groups as indicated by a more visible peak at 1421 cm^{-1}. The carboxyl groups still existed after the immobilization. With the conjugation of glycine or tetrapeptide, the typical C—O—C glycosidic linkage bands at 491, 510, 560, 1090 and 1115 cm^{-1} showed no obvious change (Q. Li & Renneckar, 2011). On the other hand, the peak at 1241 cm^{-1} assigned to the C—OH deformation dramatically decreased in both the DCNC-pep and WCNF-pep, indicating the substitution of peptide on the hydroxyl groups of NCs (Adebajo, Frost, Kloprogge, & Kokot, 2006). Also, the disorder of OH groups on C6 position is apparent by the decreased peak at 891 cm^{-1} accompanied with generation of band at 805 cm^{-1} and 855 cm^{-1} that are typical signals of amino acids (Ikoma, Kobayashi, Tanaka, Walsh, & Mann, 2003). Thus ATR-FTIR and Raman spectra confirm formation of the targeted peptide-cellulose conjugate.

3.3. Surface properties and peptide substitution

SSA of cellulose materials is considered to be an important factor for peptide immobilization. A high SSA may increase the number of hydroxymethyl groups that are available for chemical modification (Edwards, Fontenot, Haldane et al., 2016; Edwards, Fontenot, Prevost et al., 2016). Fig. 3a and b presents the surface properties including SSA, average pore diameter and surface charge. Nitrogen adsorption experiments at 77 K revealed that the BET SSA of DCNCs and WCNFs were 2.409 m^2/g and 6.895 m^2/g respectively. The value for wood is lower than the SSA previously determined, and is attributed to aggregation due to freeze drying of the nanocrystal prior to immobilization of the peptide. However, it is notable that these nanocellulosic matrices provide transducer surfaces 1000 time higher than those previously determined with cotton cellulose in the form of print cloth and filter paper which have been examined for protease sensor activity as well (Edwards et al., 2018; Fontenot et al., 2016). In addition, both NC samples presented nano sized pore diameters as well. DCNCs had an average adsorption pore diameter of 15.89 nm that is in the range for micropores, while the pore diameter of WCNF was found to be slightly higher at 20.04 nm which is within the range of micropores and mesopores (Groen, Peffer, & Pérez-Ramírez, 2003). Interestingly a high density of mesopores has been correlated with improved peptide adsorption efficiency on materials and is also relevant to ionic strength and molecular weight (Kopecka, Pivokonsky, Pivokonska, Hnatukova, & Safarikova, 2014). Moreover materials having a large number of mesopores have been shown to correlate with improved peptide adsorption efficiency on materials. These observations are relevant to the

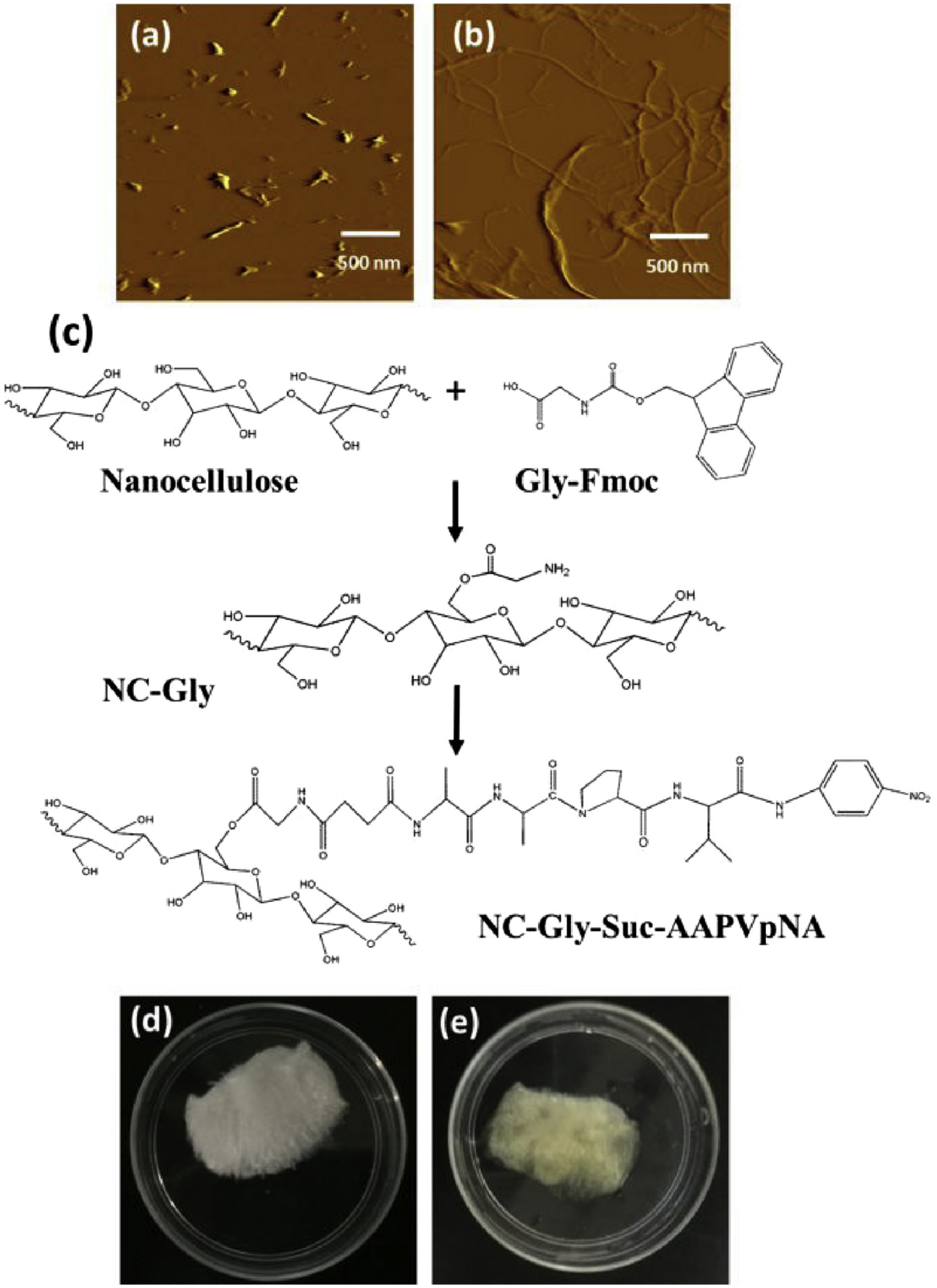

Fig. 1. Height images of DCNCs (a) and WCNFs (b) in dried suspension; Synthesis of the DCNC/WCNF peptide conjugate: Succinyl-Ala-Ala-Pro-Val-para-nitroanilide is reacted with glycine-NC (c); The HNE hydrolysis of peptide (d) yields pNA which is visibly yellow (e) can be amplified by a microplate reader (For interpretation of the references to colour in this figure legend, the reader is referred to the web version of this article).

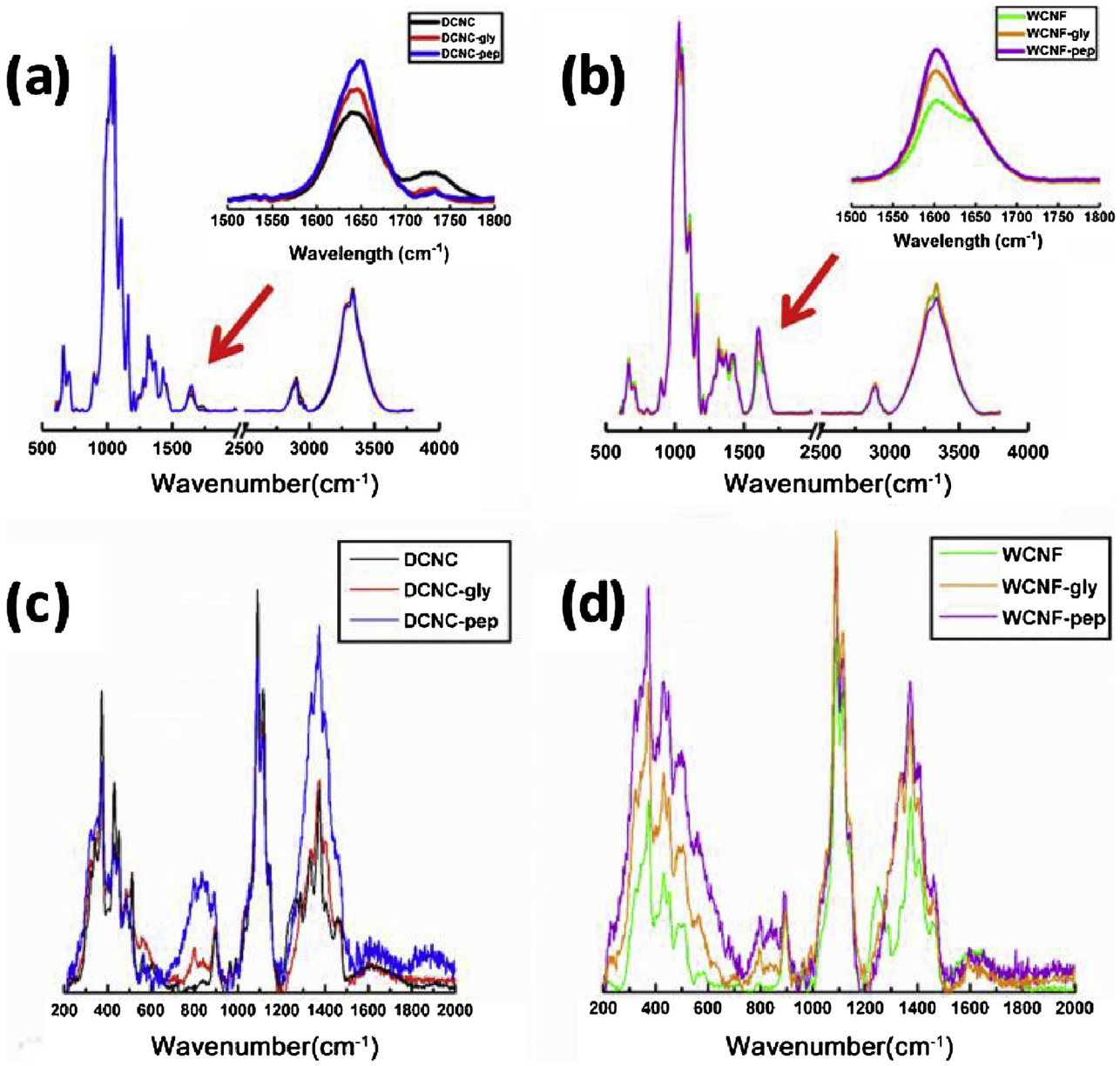

Fig. 2. ATR-FTIR spectra of DCNCs, DCNC-gly, DCNC-pep (a) and WCNFs, WCNF-gly, WCNF-pep (b); Raman spectra of DCNCs, DCNC-gly, DCNC-pep (c) and WCNFs, WCNF-gly, WCNF-pep (d).

work reported here. However the high titre of carboxylates occupying putative reaction sites at the hydroxymethyls abrogates formation of the glycine ester of cellulose. Thus the higher BET/SSA and the structure of WCNFs with predominantly mesopores are thought to improve immobilization of the HNE substrate peptide.

The morphology of NC and NC-peptide are contrasted with FE-SEM images (Fig. 3c–f). After freeze-drying, the FE-SEM images of DCNCs exhibited a lamellar structure, with aggregations of small crystals on the surface. The images of WCNFs are indicative of self-assembly of nanocrystals into macro fibrils displaying a coarse structure. Moreover, the nanofibrils of the TEMPO-oxidize wood cellulose give a relatively high surface area and more are disposed for improved immobilization of the peptide to form the peptide-cellulose conjugate. On the other hand, with regard to DCNC-pep and WCNF-pep the images shown in Fig. 3d and f reflect the presence of regions along the lamellar surface visible as 'white spots' in the FE-SEM image which are likely due to aggregates of peptide-cellulose conjugate, and these appear in greater density in the images of DCNC-pep than with WCNF-pep. The presence of these images is consistent with these distinct areas due to peptide aggregates since it correlates with quantitative incorporation of peptide in the nanocellulosic matrices. By way of correlating these regions in the images with the occurrence of peptide in the nanofibril structure it appears that the peptide on WCNF-pep appears predominantly on spots attached randomly on the DCNC-pep and WCNF-pep, suggesting the immobilization of tetrapeptide on both samples (Fig. 3d and f). There were more spots distributed on the surface of DCNC-pep while WCNF-pep had fewer spots attached in the same magnification area. The peptide on WCNF-pep covered on the edge of the layers, which may be caused by different particle sizes and surface area of freeze dried NC.

The level of peptide conjugation was determined to evaluate the level of sensor molecule quantitatively incorporated by way of covalent attachment to NC samples. The percentage of nitrogen in the Gly-cellulose conjugates present in the samples was found to be highest in the WCNC-Gly sample (Fig. 3g, h). However upon attachment of the peptide to form WCNC-pep and DCNC-pep it was found that incorporation was highest in DCNC-pep i.e. the conjugation of tetrapeptide on NC

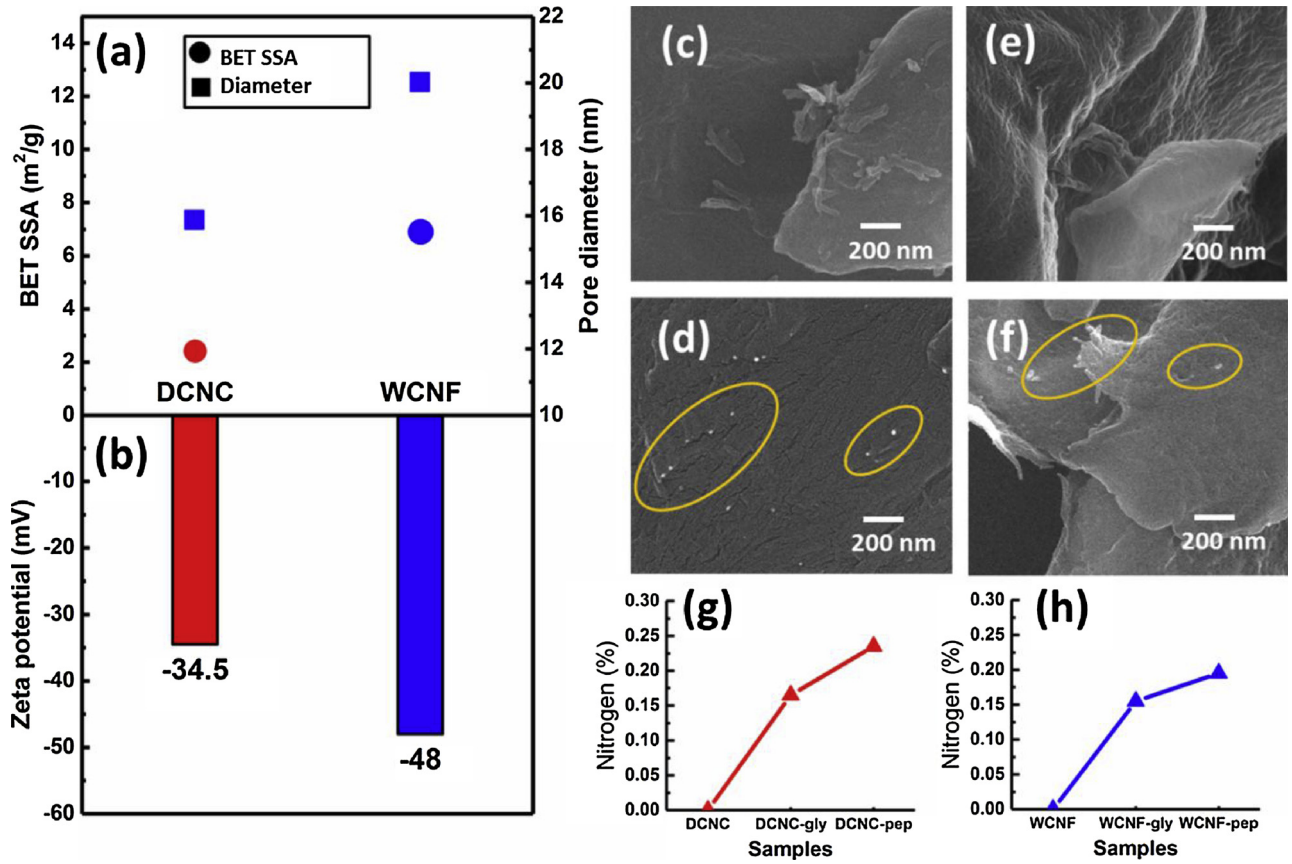

Fig. 3. Average specific surface area (SSA) (square) and pore sizes (circle) (a); Surface charges of NC (b); FE-SEM images of DCNC (c), DCNC-pep (d), WCNF (e) and WCNF-pep (f), the orange circles indicate the peptide attached on the surfaces of NC; Nitrogen element concentration variations in DCNC (g) and WCNF (h) samples. (For interpretation of the references to colour in this figure legend, the reader is referred to the web version of this article).

Table 1
Cellulose peptide levels of incorporation on DCNC and WCNF.

Samples	Nitrogen mass (ug)	Peptide mass (ug)	Peptide/ Sensor (ug/ mg)	Degree of substitution (%)
DCNC-gly	15.29	–[b]	–	0.2282
DCNC-pep	11.38	71.09	62.50	0.1767
WCNF-gly	17.56	–	–	0.2620
WCNF-pep	6.26	39.10	34.38	0.0972

[a]Nitrogen calculation of NC-peptide does not include the nitrogen in NC-gly.
[b]The peptide mass and ratio were not calculated for NC-gly.

varied from 34.4 to 62.5 μg/gram for DCNC-pep and WCNC-pep respectively. Thus, the degree of substitution for peptide incorporation is nearly twice as high in DCNC-pep (0.1767) compared to WCNC-pep (0.0972) (Table 1). The higher D.S observed for DCNC-pep versus WCNF-pep may be due to truncated glycine esters resulting from formation a amide bond forming side reaction by way of the alpha amino of the glycine ester with activated O-acyl-isoureas of adjacent carboxylates in TEMPO-oxidized cellulose during conjugation. Although this may have also occurred with the DCNC-pep reaction as well there are fewer free carboxylates to give rise to this. However, the high degree of carboxylation on the C6 position in the WCNFs is consistent with the higher negative zeta potential (Fig. 3b) and this is also consistent with the ATR-FTIR and Raman spectra results discussed above. It is noteworthy that deeper TEMPO oxidation results in a lower degree of polymerization though improved fibrillation of CNFs as has been noted (Lourenço et al., 2017). Furthermore, low DS was more notable when grafting with long chain peptides on TEMPO-oxidized NCs (Siqueira, Bras, & Dufresne, 2009). Thus, overall as noted above, both surface properties as with charge and SSA, and the actual conjugation chemistry affect the DS levels observed in the NCs. Meanwhile, the extensive carboxylation at C6 of WCNF is most likely has the most predominant effect on DS of the peptide-cellulose analog.

3.4. X-Ray crystallography

To further elucidate the crystal structure of NCs and NC-pep, X-ray diffraction patterns were collected (Fig. 4a). Both NCs gave a cellulose pattern. DCNCs had sharper peaks than WCNFs due to the larger crystallite size, higher crystalline proportion. With the immobilization of HNE peptide, both DCNC-pep and WCNF-pep showed increased intensity and sharpness for the peaks at $2\theta = 34.5^{\circ}$ corresponding to several reflections of cellulose Iβ, which suggested the more randomly arranged crystals after peptide attachment. The shoulder peak at around $2\theta = 20.5^{\circ}$ for overlapped (012) and (102) reflections was more visible for DCNC-pep. It confirmed less crystals with preferred orientation after the immobilization, which probably resulted from aggregation of the long-chain peptide (French, 2014). However, this phenomenon is not obvious for WCNF-pep with more amorphous regions in the material (Fig. 4c).

As reported earlier, the attachment mainly took place on the C6 position which occurs on the hydrophilic (1–10) and (110) reflections (Besombes & Mazeau, 2005). The crystallite sizes of each sample were based on the fitting results from Maud (Fig. S2). As seen in Fig. 4b, the crystallite size perpendicular to these two planes showed great difference that DCNC samples had much bigger crystals than WCNFs, which were derived from the variations inherent in the raw materials, cotton and wood. For DCNCs, a larger crystallite size provided more accessibility for reaction, accelerating the linkage of peptide even though a

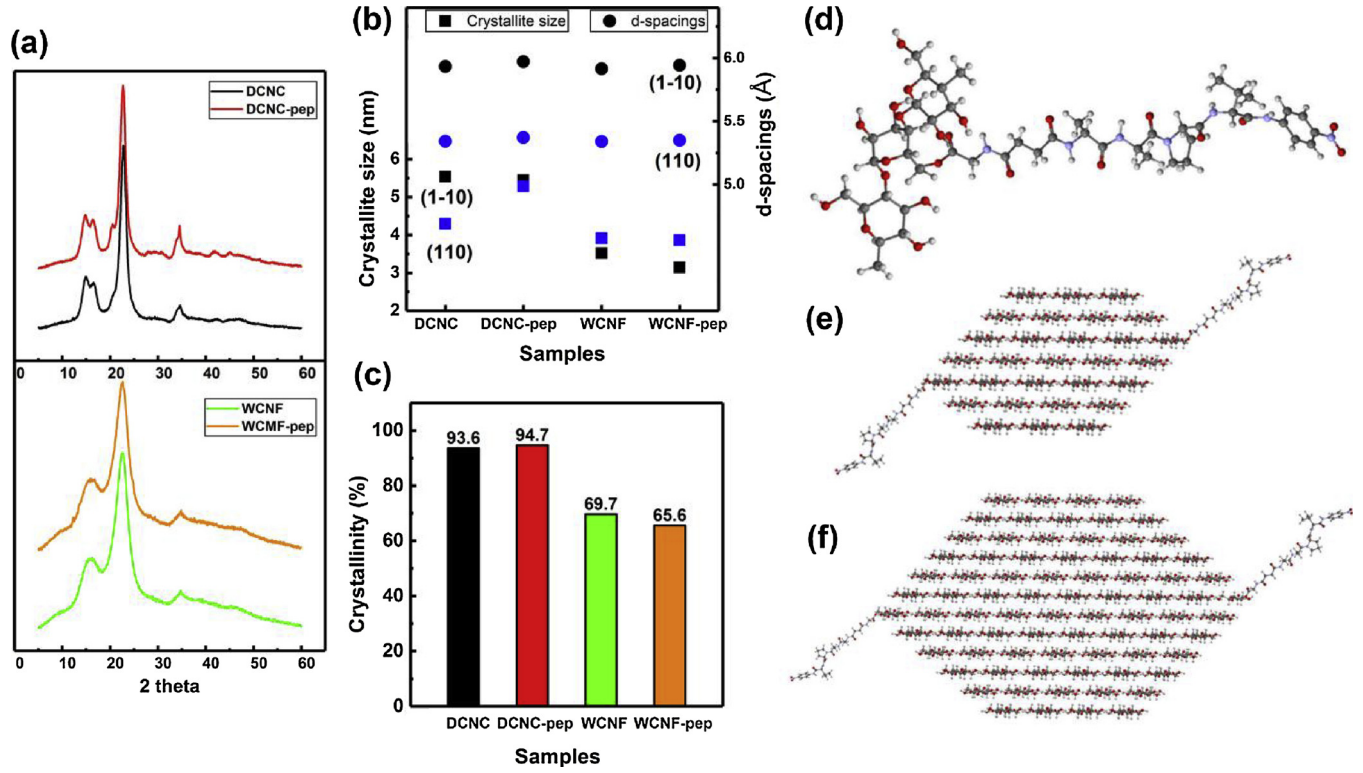

Fig. 4. XRD patterns (a), crystal structure calculation (b) and crystallinity (c) of DCNCs, DCNC-pep, WCNFs and WCNF-pep; (d): The minimum energy conformations of tetrapeptide (Suc-AAPVpNA) coupled to glycine-ester- cellotriose; (e): schematic model for tetrapeptide linked to WCNF on the (110) reflection of the crystal; (f) schematic model for tetrapeptide linked to DCNC on the (110) reflection of the crystal, WCNF had much smaller crystallite sizes than DCNC, leading to less attachments of the tetrapeptide.

smaller SSA was detected compared to WCNFs. There was a notable increase of crystallite size perpendicular to (110) lattice plane of DCNC-pep than for DCNCs whereas the WCNFs showed only slight changes that resulted from conjugation. The higher DS of tetrapeptide was revealed for DCNC-pep. Moreover, the more aggregation of peptides on the surface of DCNC-pep than WCNF-pep is considered to disturb the arrangement of crystals, thus increasing the crystallite size. It can be concluded that, the more hydrophilic (110) lattice plane of NC was the main surface for peptide immobilization due to more hydroxymethyl groups exposed on this reflection (Biermann, Hädicke, Koltzenburg, & Müller-Plathe, 2001). The result agrees with our former computational modelling study on a tripeptide on cellotriose (Edwards, Fontenot, Prevost et al., 2016). For D-spacings of each reflection, there was a slight increase before and after the immobilization, indicating that the linkage of peptide may pull the layers at the direction vertical to each lattice plane together with the expanding of crystallite size.

3.5. Molecular modelling study

The energy minimization for tetrapeptide (Suc-AAPVpNA) linked to glycine based on the cellotriose model was obtained by Gaussian 16 software (Fig. 4d–f). The disposition of the molecular models suggests some conformational differences in the sensor peptide conjugate that may be caused by interactions with the surface of the NCs versus the peptide analog in solution. The β-turn conformation for tetrapeptide was observed from the minimization, which is consistent with recently reported conformation for tripeptide (Edwards et al., 2018). The β-turn conformation tends to form in more hydrophobic and proteinaceous environments, which also provided a high affinity for the transducer surface. The schematic model for DCNC-pep and WCNF-pep were illustrated according to the XRD calculations. The increasing crystallite size on (110) reflection of the crystal indicates the linkage of the peptide on the C6 position of this lattice plane (Fig. 4e and f). The 7 layers and 12 layers were respectively calculated from crystallite size and D-spacing's for WCNF-pep and DCNC -pep on the (110) reflection. DCNCs had a larger crystallite size as well as D-spacing when compared with WCNFs. As a result, more activated hydroxymethyl group and the space were available for DCNCs, which in turn, facilitating the conjugation of glycine as well as the tetrapeptide on the surface of the materials.

3.6. HNE sensitivity and colorimetric amplification

Recently reports on utilizing approaches to adopting point of care protease level detection for chronic wound treatment have focused on description of the sensitivity and specificity of protease levels in terms of identifying chronic (non-healing) and healing wounds (Serena et al., 2016). Analysis of protease levels performed in a study of clinical classifications of chronic wounds showed that the minimum elevation in HNE levels in a chronic wound is within the range of 0.35–0.78 mU/110 µl. In Fig. 5a, the concentration dependent relationship of the colorimetric response for the two chromogenic sensors at 1 mg of the DCNC and WCNF, based on the peptide-cellulose conjugate, is a range of HNE unit's representative of chronic wounds and of the levels cited in the Serena paper and other inflammatory diseases. It is apparent that a visible colour at as low 0.025 U/mL is sufficient to visually detect HNE concentrations within the range found in chronic wounds. On the other hand spectroscopic detection of HNE was observed at 0.005 U/m, which exceeds visible wavelength detection levels of sensitivity previously reported (Stair, Watkinson, & Krause, 2009).

A variety of reports citing elastase activity in chronic wounds have been addressed in the literature and associated with deleterious effects. In light of this it is important to note that elastase activity is often expressed differently. For example, Trengove et al. reported elastase activity as having median levels of 100–110 g/mL (Trengove et al., 1999). Cullen et al. reported elastase activity in the chronic wound in relative fluorescence units (456 RFU/min/mg protein) (Cullen, Smith,

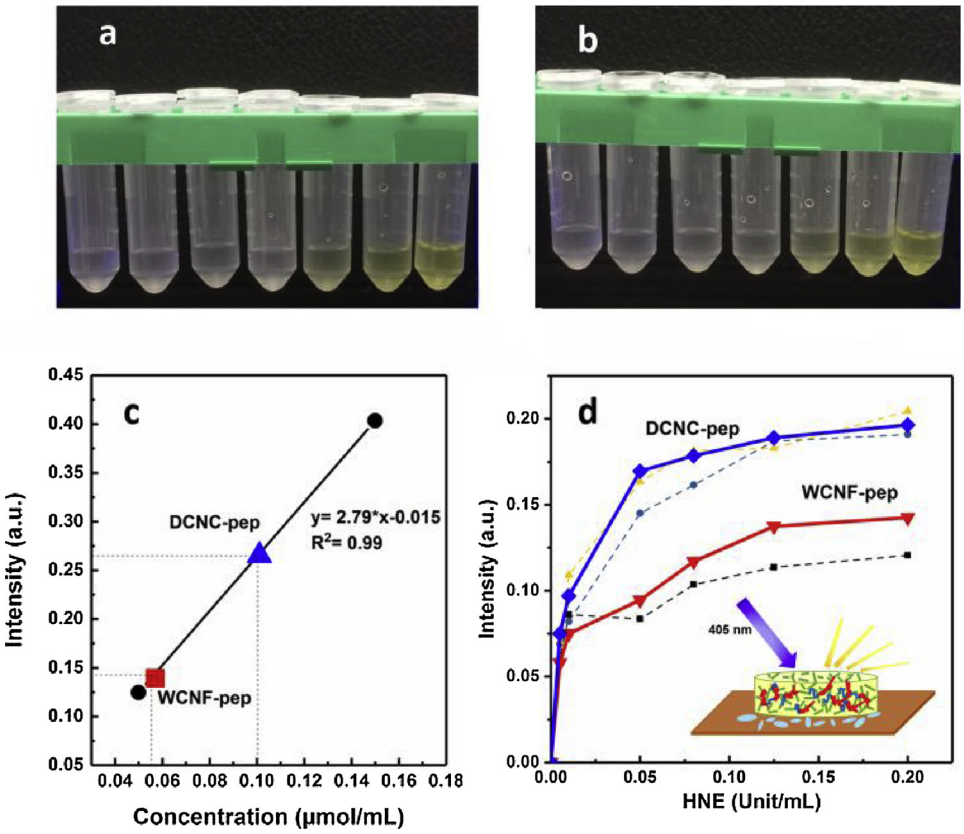

Fig. 5. Colorimetric amplification upon HNE (0, 0.005, 0.01 0.05, 0.08, 0.125 and 0.2 U/mL) substrate hydrolysis on 1 mg of (a) DCNC-pep and (b) WCNF-pep; (c) The linear fitting of intensity at 405 nm wavelength and the concentration of para-nitroanilide released by the 0.5 U/mL HNE; (d) Intensity at 405 nm wavelength with different HNE concentration, compared with standard curves of 0.02, 0.08 and 0.2 μmol/mL of AAPVpNA.

Mcculloch, Silcock, & Morrison, 2002). Yager et al reported elastase activity in chronic wound fluid as 1 mU/mg protein (Yager et al., 1997). Interestingly, the Yager report is consistent with the recent clinical study by Serena et al. (2016) in terms of differentiating a chronic non-healing wound from one that has a trajectory for healing. Elastase activity in pressure and leg ulcers show that elastase activity ranges from 1 to 50 milliunits and in acute healing wounds it is approximately 0.1 milliunits, with a unit of enzyme activity being defined as it is in this paper. As seen in Fig. 5, the amount of detectable HNE is within the limits of reported HNE activity present in chronic wound fluid (50 mU HNE) and observable with both colour complexes. However this is the upper limit of activity reported in the literature, and further work will need to be done to access the lower ranges of HNE detection sensitivity with this biosensor.

4. Conclusions

In this work, DCNCs that were fabricated by ChCl/OA treatment and TEMPO-oxidized WCNFs were decorated with a protease sensitive peptide for detection of HNE. Suc-AAPVpNA was covalently attached to glycine esterified DCNCs and WCNFs. The colorimetric detection of HNE with NCs peptide conjugates was sensitive at HNE levels in human inflammatory diseases such as chronic wound and lung disease. DCNCs showed higher degree of substitution than WCNFs, which in turn displayed better bioactivity for colorimetric detection. Even though WCNFs had higher surface area and larger pore sizes, the greater number of carboxylic groups induced by TEMPO oxidation caused high negative charge on the surface and hindered the conjugation of longer chain peptide to the glycine esterified C6 group of WCNFs. Also, the higher crystallinity and crystallite sizes of DCNCs provided well-arranged crystallite chains for immobilization of tetrapeptide that took place mainly on the (110) lattice planes of NCs crystals. The DCNCs from new facile solvent treatment and WCNFs from TEMPO oxidation were proved to be ideal materials assembled to protease biosensors. They showed potential use for wound dressing as well as an in situ diagnostic point of care assessment for HNE in inflammatory diseases.

Acknowledgements

The authors gratefully acknowledged financial support by National Key Research and Development Program of China (2017YFD0601004) and Chinese Scholarship Council (CSC No. 201706510045). We also appreciate Dr Casey Grimm of USDA for mass spectral analysis.

Appendix A. Supplementary data

Supplementary material related to this article can be found, in the online version, at doi:https://doi.org/10.1016/j.carbpol.2019.04.027.

References

Adebajo, M. O., Frost, R. L., Kloprogge, J. T., & Kokot, S. (2006). Raman spectroscopic investigation of acetylation of raw cotton. *Spectrochimica Acta Part A: Molecular and Biomolecular Spectroscopy, 64*(2), 448–453.

Besombes, S., & Mazeau, K. (2005). The cellulose/lignin assembly assessed by molecular modeling. Part 1: Adsorption of a threo guaiacyl β-O-4 dimer onto a Iβ cellulose whisker. *Plant Physiology and Biochemistry, 43*(3), 299–308.

Biermann, O., Hädicke, E., Koltzenburg, S., & Müller-Plathe, F. (2001). Hydrophilicity and lipophilicity of cellulose crystal surfaces. *Angewandte Chemie International Edition, 40*(20), 3822–3825.

Chung, C., Lee, M., & Choe, E. K. (2004). Characterization of cotton fabric scouring by FT-IR ATR spectroscopy. *Carbohydrate Polymers, 58*(4), 417–420.

Cullen, B., Smith, R., Mcculloch, E., Silcock, D., & Morrison, L. (2002). Mechanism of action of PROMOGRAN, a protease modulating matrix, for the treatment of diabetic foot ulcers. *Wound Repair and Regeneration, 10*(1), 16–25.

Dabiri, G., Damstetter, E., & Phillips, T. (2016). Choosing a wound dressing based on common wound characteristics. *Advances in Wound Care, 5*(1), 32–41.

Edwards, J. V., Fontenot, K., Liebner, F., French, A. D., & Condon, B. D. (2018). Structure/Function analysis of cotton-based peptide-cellulose conjugates: Spatiotemporal/Kinetic assessment of protease aerogels compared to nanocrystalline and paper cellulose. *International Journal of Molecular Sciences, 19*(3), 840.

Edwards, J. V., Prevost, N., Sethumadhavan, K., Ullah, A., & Condon, B. (2013). Peptide conjugated cellulose nanocrystals with sensitive human neutrophil elastase sensor

activity. *Cellulose, 20*(3), 1223–1235. https://doi.org/10.1007/s10570-013-9901-y.
Edwards, J. V., Fontenot, K. R., Haldane, D., Prevost, N. T., Condon, B. D., & Grimm, C. (2016). Human neutrophil elastase peptide sensors conjugated to cellulosic and nanocellulosic materials: Part I, synthesis and characterization of fluorescent analogs. *Cellulose*. https://doi.org/10.1007/s10570-016-0869-2.
Edwards, J. V., Fontenot, K. R., Prevost, N. T., Pircher, N., Liebner, F., & Condon, B. D. (2016). Preparation, characterization and activity of a peptide-cellulosic aerogel protease sensor from cotton. *Sensors (Basel, Switzerland), 16*(11), 1–19. https://doi.org/10.3390/s16111789.
Eshraghi, J., & Chowdhury, S. K. (1993). Factors affecting electrospray ionization of effluents containing trifluoroacetic acid for high-performance liquid chromatography/mass spectrometry. *Analytical Chemistry, 65*(23), 3528–3533.
Fontenot, K. R., Edwards, J. V., Haldane, D., Graves, E., Citron, M. S., Prevost, N. T., ... Condon, B. D. (2016). Human neutrophil elastase detection with fluorescent peptide sensors conjugated to cellulosic and nanocellulosic materials: Part II, structure/function analysis. *Cellulose*. https://doi.org/10.1007/s10570-016-0873-6.
Fontenot, K. R., Edwards, J. V., Haldane, D., Pircher, N., Liebner, F., Condon, B. D., ... Yager, D. (2017). Designing cellulosic and nanocellulosic sensors for interface with a protease sequestrant wound-dressing prototype: Implications of material selection for dressing and protease sensor design. *Journal of Biomaterials Applications, 32*(5), 622–637. https://doi.org/10.1177/0885328217735049.
French, A. D. (2014). Idealized powder diffraction patterns for cellulose polymorphs. *Cellulose, 21*(2), 885–896. https://doi.org/10.1007/s10570-013-0030-4.
Groen, J. C., Peffer, L. A. A., & Pérez-Ramírez, J. (2003). Pore size determination in modified micro- and mesoporous materials. Pitfalls and limitations in gas adsorption data analysis. *Microporous and Mesoporous Materials, 60*(1–3), 1–17. https://doi.org/10.1016/S1387-1811(03)00339-1.
Habibi, Y., Lucia, L. A., & Rojas, O. J. (2010). Cellulose nanocrystals: Chemistry, self-assembly, and applications. *Chemical Reviews, 110*(6), 3479–3500. https://doi.org/10.1021/cr900339w.
Holzwarth, U., & Gibson, N. (2011). The Scherrer equation versus the'Debye-Scherrer equation'. *Nature Nanotechnology, 6*(9), 534.
Ikoma, T., Kobayashi, H., Tanaka, J., Walsh, D., & Mann, S. (2003). Physical properties of type I collagen extracted from fish scales of Pagrus major and Oreochromis niloticas. *International Journal of Biological Macromolecules, 32*(3–5), 199–204.
Jorfi, M., & Foster, E. J. (2015). Recent advances in nanocellulose for biomedical applications. *Journal of Applied Polymer Science, 132*(14).
Kopecka, I., Pivokonsky, M., Pivokonska, L., Hnatukova, P., & Safarikova, J. (2014). Adsorption of peptides produced by cyanobacterium Microcystis aeruginosa onto granular activated carbon. *Carbon, 69*, 595–608. https://doi.org/10.1016/j.carbon.2013.12.072.
Langan, P., Nishiyama, Y., & Chanzy, H. (2001). X-ray structure of mercerized cellulose II at 1 ! Resolution X-ray structure of mercerized cellulose II at 1 Å resolution. *Cellulose, 2*(April), 410–416. https://doi.org/10.1021/bm005612q.
Li, Q., & Renneckar, S. (2011). Supramolecular structure characterization of molecularly thin cellulose i nanoparticles. *Biomacromolecules, 12*(3), 650–659. https://doi.org/10.1021/bm101315y.
Li, B., Xu, W., Kronlund, D., Määttänen, A., Liu, J., Smått, J. H., ... Xu, C. (2015). Cellulose nanocrystals prepared via formic acid hydrolysis followed by TEMPO-mediated oxidation. *Carbohydrate Polymers, 133*, 605–612. https://doi.org/10.1016/j.carbpol.2015.07.033.
Liao, L.-F., Lien, C.-F., Shieh, D.-L., Chen, F.-C., & Lin, J.-L. (2002). FTIR study of adsorption and photochemistry of amide on powdered TiO 2: Comparison of benzamide with acetamide. *Journal of the Chemical Society Faraday Transactions, 4*(18), 4584–4589.
Ling, Z., Chen, S., Zhang, X., & Xu, F. (2017). Exploring crystalline-structural variations of cellulose during alkaline pretreatment for enhanced enzymatic hydrolysis. *Bioresource Technology, 224*, 611–617. https://doi.org/10.1016/j.biortech.2016.10.064.
Ling, Z., Edwards, J. V., Guo, Z., Prevost, N. T., Nam, S., Wu, Q., ... Xu, F. (2018). Structural variations of cotton cellulose nanocrystals from deep eutectic solvent treatment: Micro and nano scale. *Cellulose, 9*. https://doi.org/10.1007/s10570-018-2092-9.
Ling, Z., Zhang, X., Yang, G., Takabe, K., & Xu, F. (2018). Nanocrystals of cellulose allomorphs have different adsorption of cellulase and subsequent degradation. *Industrial Crops and Products, 112*, 541–549.
Lourenço, A. F., Gamelas, J. A. F., Nunes, T., Amaral, J., Mutjé, P., & Ferreira, P. J. (2017). Influence of TEMPO-oxidised cellulose nanofibrils on the properties of filler-containing papers. *Cellulose, 24*(1), 349–362. https://doi.org/10.1007/s10570-016-1121-9.
Nam, S., French, A. D., Condon, B. D., & Concha, M. (2016). Segal crystallinity index revisited by the simulation of X-ray diffraction patterns of cotton cellulose I-β and cellulose II. *Carbohydrate Polymers, 135*, 1–9. https://doi.org/10.1016/j.carbpol.2015.08.035.
Nishiyama, Y., Langan, P., & Chanzy, H. (2002). Crystal structure and hydrogen-bonding system in cellulose Iβ from synchrotron X-ray and neutron fiber diffraction. *Journal of the American Chemical Society, 124*(31), 9074–9082.
Orlandin, A., Formaggio, F., Toffoletti, A., & Peggion, C. (2014). Cotton functionalized with peptides: Characterization and synthetic methods. *Journal of Peptide Science, 20*(7), 547–553.
Owen, C. A. (2008). Roles for proteinases in the pathogenesis of chronic obstructive pulmonary disease. *International Journal of Chronic Obstructive Pulmonary Disease, 3*(2), 253.
Romanelli, M., Miteva, M., Romanelli, P., Barbanera, S., & Dini, V. (2013). Use of diagnostics in wound management. *Current Opinion in Supportive and Palliative Care, 7*(1), 106–110.
Salas, C., Nypelö, T., Rodriguez-Abreu, C., Carrillo, C., & Rojas, O. J. (2014). Nanocellulose properties and applications in colloids and interfaces. *Current Opinion in Colloid & Interface Science, 19*(5), 383–396.
Serena, T. E., Cullen, B. M., Bayliff, S. W., Gibson, M. C., Carter, M. J., Chen, L., ... DeMarco, D. (2016). Defining a new diagnostic assessment parameter for wound care: Elevated protease activity, an indicator of nonhealing, for targeted protease--modulating treatment. *Wound Repair and Regeneration, 24*(3), 589–595.
Sibrian-Vazquez, M., Jensen, T. J., Hammer, R. P., & Vicente, M. G. H. (2006). Peptide-mediated cell transport of water soluble porphyrin conjugates. *Journal of Medicinal Chemistry, 49*(4), 1364–1372.
Siqueira, G., Bras, J., & Dufresne, A. (2009). New process of chemical grafting of cellulose nanoparticles with a long chain isocyanate. *Langmuir, 26*(1), 402–411.
Sirviö, J. A., Visanko, M., & Liimatainen, H. (2016). Acidic deep eutectic solvents as hydrolytic media for cellulose nanocrystal production. *Biomacromolecules, 17*(9), 3025–3032. https://doi.org/10.1021/acs.biomac.6b00910.
Stair, J. L., Watkinson, M., & Krause, S. (2009). Sensor materials for the detection of proteases. *Biosensors & Bioelectronics, 24*(7), 2113–2118.
Trengove, N. J., Stacey, M. C., Macauley, S., Bennett, N., Gibson, J., Burslem, F., ... Schultz, G. (1999). Analysis of the acute and chronic wound environments: The role of proteases and their inhibitors. *Wound Repair and Regeneration, 7*(6), 442–452.
Wang, S., Lu, A., & Zhang, L. (2016). Progress in polymer science recent advances in regenerated cellulose materials. *Progress in Polymer Science, 53*, 169–206. https://doi.org/10.1016/j.progpolymsci.2015.07.003.
Yager, D. R., Chen, S. M., Ward, S. I., Olutoye, O. O., Diegelmann, R. F., & Kelman Cohen, I. (1997). Ability of chronic wound fluids to degrade peptide growth factors is associated with increased levels of elastase activity and diminished levels of proteinase inhibitors. *Wound Repair and Regeneration, 5*(1), 23–32.